Nuclear Science and Techniques (2025) 36:228
https://doi.org/10.1007/s41365-025-01826-w

Study of the momentum correlation of nucleons in $^{96}_{44}$Ru + $^{96}_{44}$Ru and $^{96}_{40}$Zr + $^{96}_{40}$Zr collisions at $\sqrt{s_{\mathrm{NN}}}$ = 7.7 and 200 GeV from a multiphase transport model

Bao-Shan Xi[1,2] · Jin-Hui Chen[1,2] · Long Ma[1,2] · Yu-Gang Ma[1,2] · Ting-Ting Wang[3]

Received: 1 July 2025 / Revised: 18 August 2025 / Accepted: 26 August 2025 / Published online: 29 September 2025

Abstract
By using a multiphase transport (AMPT) model in the string melting scenario, the influences of nuclear structure on the momentum correlation functions between nucleons in the isobaric collisions of $^{96}_{44}$Ru + $^{96}_{44}$Ru and $^{96}_{40}$Zr + $^{96}_{40}$Zr at $\sqrt{s_{\mathrm{NN}}}$ = 7.7 and 200 GeV were investigated. The results, including the centrality dependence of the correlation functions, were compared across different parameterizations of the Woods–Saxon distribution corresponding to varying deformation configurations in the simulation. A maximum difference of 4% was observed between the isobaric systems for the proton–proton correlation functions when including quadrupole (β_2) and octupole (β_3) deformation. In peripheral collisions, the Ru + Ru and Zr + Zr systems exhibited maximum differences of 4% and 5%, respectively, when comparing different parametrization cases. Furthermore, neutron–proton correlation has been studied, showing a sensitivity to nuclear structure comparable to proton–proton correlations. Our results indicate that in peripheral collisions, there may be measurable effects of momentum correlation functions from nuclear deformation and neutron skin in high-precision experimental data, whereas in central collisions, both effects may show negligible influence on momentum correlation functions.

Keywords Momentum correlation · Nuclear deformation · Heavy-ion collision

1 Introduction

Relativistic heavy-ion collisions provide a unique laboratory for studying quantum chromodynamics (QCD) under extreme conditions, including the formation of quark–gluon plasma (QGP) [1]. Extensive studies have been conducted at both RHIC and LHC energies across various collision systems to investigate the properties of the QGP matter [2–7]. Among various collision systems, isobaric collisions, such as $^{96}_{44}$Ru + $^{96}_{44}$Ru and $^{96}_{40}$Zr + $^{96}_{40}$Zr, proposed experimentally for the search of the anomalous phenomenon of the chiral magnetic effect (CME), also offer an effective tool for investigating the influence of the initial nuclear structure on final-state observables, such as anisotropic flow [8–10]. The upgrade of detectors also provides new avenues for exploring the CME [11–13]. These collision systems have identical mass numbers, but differ in nuclear deformation and density distributions, making them ideal for isolating deformation effects from other variables [14–19]. Notably, Ru nuclei exhibit quadrupole deformation, whereas Zr nuclei

This work was supported by the National Key R&D Program of China (No. 2022YFA1604900), National Natural Science Foundation of China (No. 12025501), and National Natural Science Foundation of China (No. 12147101).

✉ Long Ma
malong@fudan.edu.cn

✉ Yu-Gang Ma
mayugang@fudan.edu.cn

[1] Institute of Modern Physics, Fudan University, Shanghai 200433, China

[2] Key Laboratory of Nuclear Physics and Ion-beam Application(MOE), Fudan University, Shanghai 200433, China

[3] Shanghai Institute of Applied Physics, Chinese Academy of Sciences, Shanghai 201800, China

display octupole deformation. By comparing these systems, researchers can disentangle the initial-state geometry from medium-induced effects, offering deeper insights into the QGP properties as well as the nuclear structure [20, 21]. As recently reported in the results of the STAR experiment, differences were observed in the elliptic flow coefficient (v_2) and triangular flow coefficient (v_3) ratios between the two isobaric collision systems at $\sqrt{s_{\rm NN}} = 200$ GeV, revealing the nuclear structure effects on source collectivity [8].

The two-particle momentum correlation function, known as femtoscopy, originating from Hanbury Brown–Twiss (HBT) interferometry [22], is a powerful tool for accessing the expanding source dynamics of heavy-ion physics [23–27]. Femtoscopy in relativistic heavy-ion collisions extracts space-time information about particle emission sources and probes collision dynamics. Studies have been performed on the momentum correlation of various particle species, including mesons, nucleons, light charged particles, and even antiprotons, revealing details about source size and interaction mechanisms [28]. At LHC energies, the ALICE Collaboration precisely measured the initial energy density, effective temperature, system size, lifetime, and interactions between various hadron pairs via femtoscopy, extracted the scattering parameters, and demonstrated the feasibility of detecting three-body correlations [5, 29, 30]. Notably, momentum correlations have confirmed charge-parity-time (CPT) symmetry in proton–proton and antiproton–antiproton interactions [31]. Recent advances have extended the femtoscopy studies to exotic systems, including strange hadrons (e.g., Ω and Σ hyperons), charm hadrons (e.g., D mesons), light nuclei (e.g., deuterons, tritons), and test predictions from lattice QCD and chiral effective field theory [32–34]. Measurements have been performed for the correlations between Λ-Λ, p-Λ and p-Ω, particularly for the study of hyperon–hyperon and hyperon–nucleon interaction in dense matter [35–41]. Momentum correlation studies have also been conducted for proton–deuteron and deuteron–deuteron systems, with the scattering parameters measured, offering valuable insights into strong interactions in exotic nuclear systems [42, 43]. In addition to heavy-ion collisions, analyses have been extended to smaller collision systems with further constraints on the dynamics of particle production during high-energy collisions [44–46].

In this study, we explore the effects of nuclear structure on the momentum correlation of nucleons in isobar collisions by considering the different deformation configurations of Ru and Zr nuclei. In contrast to femtoscopy studies in non-deformed nuclear systems (e.g., Au+Au and Pb+Pb), the distinct deformation profiles of Ru (quadrupole) and Zr (octupole) nuclei in isobaric collisions introduce differences in the initial-state geometry. In addition, different nuclear deformation parameters correspond to different neutron skin thicknesses. Because two-particle correlations are sensitive to source size, comparing Ru + Ru and Zr + Zr systems can reveal how nuclear deformation affects particle emission dynamics and final-state momentum correlation, which may offer an appropriate way to explore the interplay between nuclear deformation and collective dynamics inside the QGP.

This paper is organized as follows: In Sect. 2, a multiphase transport model is described, and different cases of the Woods–Saxon parameters for Ru and Zr are introduced. In Sect. 3, the results of the momentum correlation functions of nucleon pairs for different isobaric deformation configurations are discussed. In Sect. 4, a brief summary will be given.

2 Model and methodology

2.1 The AMPT model

A multiphase transport model [47, 48] has been applied extensively and successfully to study heavy-ion collisions at relativistic energies [49–54]. In the string melting version of the model, the initial-state phase space information of partons considering fluctuating initial conditions is generated by the heavy-ion jet interaction generator (HIJING) model, where minijet partons and excited strings are produced by hard and soft processes, respectively [55]. To study the collisions of deformed nuclei, we altered the nucleon distribution, which is discussed in more detail in Sect. 2.2. The interaction between partons is then simulated by Zhang's parton cascade (ZPC) model which includes only two-body parton elastic scatterings [56]. During the hadronization process, a quark coalescence model was used to combine partons into hadrons. Then, the final-state hadronic evolution is described by a relativistic transport (ART) model that considers baryon–baryon, baryon–meson, and meson–meson elastic and inelastic scatterings, as well as resonance decay processes [57].

2.2 The nuclear deformation configuration

In AMPT, the default spatial distribution of nucleons in the nucleus rest frame is given by Woods–Saxon (WS) distribution, defined as follows [15, 58–60]:

$$\rho(r,\theta) = \frac{\rho_0}{1+\exp\left[\frac{r-R_0[1+\beta_2 Y_2^0(\theta)+\beta_3 Y_3^0(\theta)]}{a}\right]}, \tag{1}$$

where r and θ denote radial position and polar angles of nucleons, respectively. The parameters R_0 and "a" denote "radius" and the surface diffuseness parameter of the nucleus, respectively, both of which influence the initial overlap area of the collision [14, 61]. ρ_0 is the nuclear

Table 1 The Woods–Saxon parameters used for the Ru and Zr nuclei in the AMPT model

Nucleus	Ru				Zr			
Para.	R_0 (fm)	a (fm)	β_2	β_3	R_0 (fm)	a (fm)	β_2	β_3
Case 1	5.096	0.540	0	0	5.096	0.540	0	0
Case 2	5.13	0.46	0.13	0	5.06	0.46	0.06	0
Case 3	5.067	0.5	0	0	4.965	0.556	0	0
Case 4	5.09	0.46	0.162	0	5.02	0.52	0.06	0.20

Table 2 Centrality definition based on charged-particle multiplicity

	Multiplicity cut (>)							
	Ru + Ru				Zr + Zr			
7.7 GeV	Case 1	Case 2	Case 3	Case 4	Case 1	Case 2	Case 3	Case 4
0–20%	61	62	62	62	61	62	61	61
20–40%	31	33	32	33	31	33	32	32
40–60%	14	15	15	15	14	15	14	15
60–80%	6	6	6	6	6	6	6	6
200 GeV	Case 1	Case 2	Case 3	Case 4	Case 1	Case 2	Case 3	Case 4
0–20%	150	154	153	154	150	155	151	151
20–40%	69	73	71	73	69	73	69	70
40–60%	28	29	29	29	28	29	27	28
60–80%	10	10	10	10	10	10	9	10

density normalization factor, determined by nucleon number A.

The quadrupole deformation parameter β_2 and the octupole deformation parameter β_3 describe the deformation of the nucleus from a spherical shape. These parameters have been widely used in recent studies [15, 58, 62–65].

In this study, we investigated the influence of the nuclear structure on the nucleon momentum correlations in relativistic isobar collisions (Ru + Ru and Zr + Zr). Because the Woods–Saxon parameters for these two isobaric systems have not been determined, we explored four cases of parameter sets in our study, as shown in Table 1 [15, 62, 64, 66–68]. Case 1 is without deformation, and values of R_0 and "a" for Ru and Zr are set to be the same, while in case 2, Ru ($\beta_2 = 0.13$) has a bigger quadrupole deformation than Zr ($\beta_2 = 0.06$). Case 3 is based on calculations using the energy density functional theory (DFT), which also assumes that the nuclei are spherical. The differences in R_0 and "a" between Zr and Ru result in a thicker neutron skin for Zr. Case 4 also includes the deformation effect and neutron skin effect. In this study, the distribution of nucleons (protons and neutrons) inside the nuclei was initialized according to Eq. (1) based on the nuclear matter density configuration.

In the AMPT model, the shape of the initial geometry produced by collisions is primarily determined by the collision event impact parameter "b" and nuclear structure

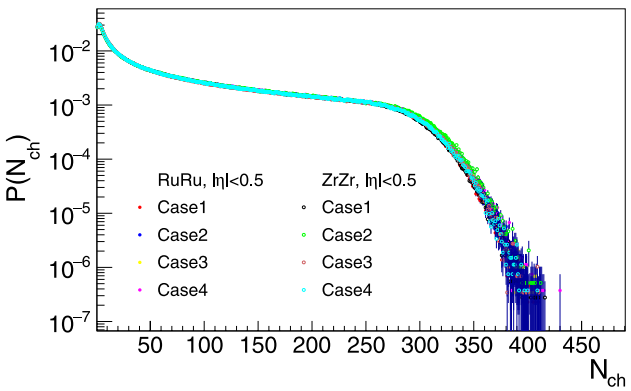

Fig. 1 (Color online) Charged-particle multiplicity distribution in mid-rapidity for Ru + Ru and Zr + Zr collisions at $\sqrt{s_{\rm NN}} = 200$ GeV. Results are compared for four different parameterization cases, shown in distinct colors

parameters. To facilitate an experimental comparison, we divided the centrality classes based on the number of final-state charged particles with pseudorapidity $|\eta| < 0.5$, instead of directly using the impact parameter. The charged-particle multiplicity distributions of the four cases of the Woods–Saxon parameterization for Ru + Ru and Zr + Zr collisions at $\sqrt{s_{\rm NN}} = 200$ GeV are shown in Fig. 1. Similar distributions with tiny differences across all four

cases were also observed for isobaric collisions at $\sqrt{s_{\rm NN}}$ = 7.7 GeV. The multiplicity intervals corresponding to different centrality classes in Ru + Ru and Zr + Zr collisions at $\sqrt{s_{\rm NN}}$ = 7.7 GeV and 200 GeV are presented in Table 2. By comparing the multiplicity distribution of various collision systems with different Woods–Saxon configurations, we note that the effect of the nuclear deformation parameters on the multiplicity distribution is small.

2.3 Correlation function

The Lednický–Lyuboshitz method [69–72] was used to calculate the momentum correlation function. Firstly, the s-wave scattering amplitude for proton–proton (p-p) pair is obtained by

$$f^S_{\rm p\text{-}p}(k^*) = \left[\frac{1}{f^S_0} + \frac{1}{2}d^S_0 k^{*2} - \frac{2}{a_{\rm c}}h\left(k^* a_{\rm c}\right) - ik^* A_{\rm c}(\eta)\right]^{-1}, \quad (2)$$

where $k^* = |\boldsymbol{k}^*|$ and $r^* = |\boldsymbol{r}^*|$ represent magnitude of half of the relative momentum difference and relative position vector between the two particles in their pair rest frames, respectively. f^S_0 denotes the scattering length and d^S_0 is the effective range. These two parameters characterize strong interactions and further determine the interactions between particles [73]. The superscript S denotes the total spin, where $S = 0$ corresponds to the singlet state, and $S = 1$ corresponds to the triplet state. $A_{\rm c}(\eta) = 2\pi\eta[\exp(2\pi\eta) - 1]^{-1}$ denotes the Coulomb penetration factor. For the p-p pair, $\eta = (k^* a_{\rm c})^{-1}$, where $a_{\rm c} = 292.1\,fm$ is the Bohr radius.

$$h(x) = \frac{1}{x^2}\sum_{n=1}^{\infty}\frac{1}{n\left(n^2 + x^{-2}\right)} - C + \ln|x|, \quad (3)$$

where $C = 0.5772$ denotes the Euler constant. Because neutrons are uncharged, there is no Coulomb interaction between the neutron and proton (n-p) pairs:

$$f^S_{\rm n\text{-}p}(k^*) = \left[\frac{1}{f^S_0} + \frac{1}{2}d^S_0 k^{*2} - ik^*\right]^{-1}. \quad (4)$$

In the following discussion, we denote $f^S_{\rm p\text{-}p}(k^*)$ and $f^S_{\rm n\text{-}p}(k^*)$ as $f^S(k^*)$. For p-p pair, the scattering length f^S_0 is 7.8 fm for singlet state and −5.4 fm for triplet state. Effective range parameter d_0 is 2.77 fm for singlet state and 1.7 fm for triplet state, while for n-p pair, the scattering length parameter f_0 is 23.7 fm and −5.4 fm, d_0 is 2.7 fm and 1.7 fm, for singlet and triplet state, respectively. The values of f_0 and d_0 in this study were obtained using the Lednický–Lyuboshitz method [69–72].

The equal-time reduced Bethe–Salpeter amplitude for p-p pair is calculated approximately as

$$\psi^{S(+)}_{-\boldsymbol{k}^*;\text{p-p}}(\boldsymbol{r}^*) = e^{i\delta_{\rm c}}\sqrt{A_{\rm c}(\eta)}\left[e^{-i\boldsymbol{k}^*\cdot\boldsymbol{r}^*}F(-i\eta, 1, i\xi) + f^S(k^*)\frac{\widetilde{G}(\rho,\eta)}{r^*}\right]; \quad (5)$$

$$\psi^{S}_{\boldsymbol{k}^*;\text{p-p}}(\boldsymbol{r}^*) = e^{i\delta_{\rm c}}\sqrt{A_{\rm c}(\eta)} \times \left[e^{i\boldsymbol{k}^*\cdot\boldsymbol{r}^*}F(-i\eta, 1, i(\rho - \boldsymbol{k}^*\cdot\boldsymbol{r}^*)) + f^S(k^*)\frac{\widetilde{G}(\rho,\eta)}{r^*}\right]. \quad (6)$$

Here F denotes the confluent hypergeometric function, $\rho = k^* r^*$ is used to describe the phase factor of plane waves and scattered spherical waves, $\xi = \boldsymbol{k}^*\cdot\boldsymbol{r}^* + \rho$ and

$$\widetilde{G}(\rho,\eta) = \sqrt{A_{\rm c}(\eta)}\left(G_0(\rho,\eta) + iF_0(\rho,\eta)\right), \quad (7)$$

where F_0 denotes the regular s-wave Coulomb function and G_0 denotes the singlet s-wave Coulomb function [69, 74, 75].

For the n-p pair, η is set to 0, and the Coulomb wave function $\widetilde{G}(\rho, 0)$ degenerates into a free spherical wave $e^{i\rho}$. Coulomb phase shift: $e^{i\delta_{\rm c}} = e^0 = 1$. The forms are as follows:

$$\psi^{S(+)}_{-\boldsymbol{k}^*;\text{n-p}}(\boldsymbol{r}^*) = e^{-i\boldsymbol{k}^*\cdot\boldsymbol{r}^*} + f^S(k^*)\frac{e^{i\rho}}{r^*}; \quad (8)$$

$$\psi^{S}_{\boldsymbol{k}^*;\text{n-p}}(\boldsymbol{r}^*) = e^{i\boldsymbol{k}^*\cdot\boldsymbol{r}^*} + f^S(k^*)\frac{e^{i\rho}}{r^*}. \quad (9)$$

The forms are denoted as $\psi^{S(+)}_{-\boldsymbol{k}^*}$ and $\psi^{S}_{\boldsymbol{k}^*}$. Incorporating these terms, the weight of the particle pair can be obtained as

$$w\left(\boldsymbol{k}^*, \boldsymbol{r}^*\right) = \sum_S R_S\left\langle\left|\psi^{S(+)}_{-\boldsymbol{k}^*}(\boldsymbol{r}^*)\right|^2\right\rangle_S, \quad (10)$$

assuming that particles were unpolarized. We set $R_0 = 1/4$ and $R_1 = 3/4$ for the pairs in the singlet and triplet states, respectively. Finally, for both p-p and n-p pairs, the theoretical correlation function can be written as:

$$C_{\rm NN}(k^*) = \frac{\sum_{\rm pairs}\delta\left(k^*_{\rm pair} - k^*\right)w\left(\boldsymbol{k}^*, \boldsymbol{r}^*\right)}{\sum_{\rm pairs}\left(k^*_{\rm pair} - k^*\right)}. \quad (11)$$

where $k^*_{\rm pair}$ denotes the actual relative momentum of a real pair in its resting frame.

3 Results and discussion

Based on the centrality definition and initial nuclear configuration described above, we studied the nucleon momentum correlation in the Ru and Zr collision systems.

The final-state phase space information can be obtained from the AMPT model for collisions with different deformed nuclei. We derived the correlation functions of p-p and n-p for four cases of nuclear deformation in different centrality classes in isobaric collisions at $\sqrt{s_{\rm NN}} = 7.7$ and 200 GeV. For the protons and neutrons selected for pair correlation, a fundamental particle cut criterion ($|p_{\rm T}| > 0.2$ GeV/c, $|\eta| < 1.0$ and $p < 10$ GeV/c) was applied.

Figure 2 shows the AMPT results of the p-p correlation functions for Ru + Ru and Zr + Zr collisions at $\sqrt{s_{\rm NN}} = 7.7$ GeV. The data points in different colors represent the results

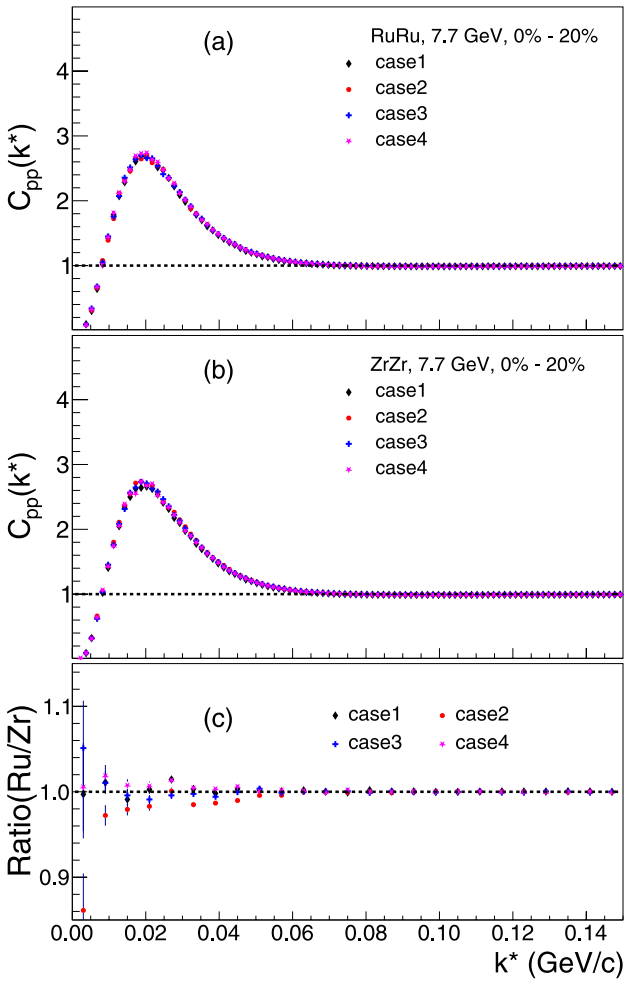

Fig. 2 Proton–proton correlation function for 0–20% central Ru + Ru (Panel a) and Zr + Zr (Panel b) collisions. Panel (c) shows the ratio between the two systems (Ru/Zr) for four different cases of Woods–Saxon parametrization as shown in Table 1

of the isobaric system with different deformation cases at a centrality of 0–20%. It can be seen that the differences between the correlation functions across collision systems and deformation parameters are very small. As the correlation function is highly sensitive to the fireball radius, the observed small differences in the correlation functions could be attributed to the relatively small deformation coefficients and neutron skin differences between the isobaric systems, which induce tiny variations in the initial-state geometry, and consequently, the fireball size. It is also possible that the correlation function itself is insensitive to nuclear deformation.

In panel (c) of Fig. 2, the ratios of the correlation functions are calculated for each deformation parameterization case, allowing for a quantitative study of the initial-state effects on the two collision systems. It can be seen that in case 1, the parameters of both systems are identical. Despite the difference in the number of nuclear charges between the two systems, little difference is observed between the correlation functions. Case 3 does not involve a nuclear shape change but incorporates the neutron skin effect. Our results demonstrate that the neutron skin effect caused by different density distributions of protons and neutrons might have a negligible influence on the correlation function in central collisions, consistent with the understanding that neutron skin effects are largely suppressed in central collisions, as they predominantly manifest in peripheral collisions [76].

In case 2, the ratio of the correlation functions between the two systems for 0–20% centrality is less than 1 with a 1–2% offset in the low k^* region. As β_3 is 0 for both Ru and Zr, the relative magnitude of the correlation function is determined by the radius parameter R_0 and quadrupole deformation parameter β_2. In contrast, the ratio results of case 4 are slightly larger than 1, with a relative difference of $\sim 1\%$, indicating that β_3 may have a potential influence on the correlation results. The ratios of these four cases are generally consistent with 1 at large k^* (>0.05 GeV/c), indicating that the effects of nuclear deformation are negligible in this region.

Figure 3 shows the results of the correlation functions for four different cases of deformation configuration in Ru + Ru (Panel a) and Zr + Zr (Panel b) collisions at $\sqrt{s_{\rm NN}} = 7.7$ GeV in centrality class 60–80%. Since the fireball size in peripheral collisions is smaller than central collisions, their correlation signal intensities are generally stronger than those in central collisions. For the ratios of the two systems presented in Panel (c), it is evident that within the k^* interval of 0.01−0.08 GeV/c, the ratio is less than 1 for case 2, whereas it exceeds 1 for the other three cases. The results of case 1 show little deviation from unity within statistical uncertainties. Case 2 has a maximum deviation of 2% suggesting that a smaller deformation induces a stronger correlation, while case 3, which includes differences in the

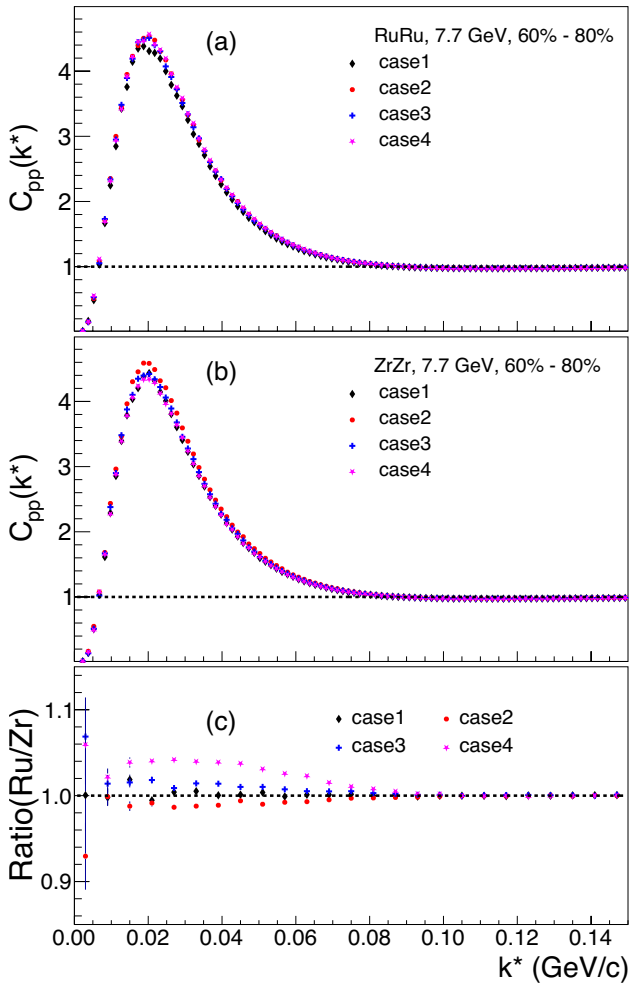

Fig. 3 Proton–proton correlation function for 60–80% central Ru + Ru (Panel a) and Zr + Zr (Panel b) collisions at center-of-mass energy $\sqrt{s_{NN}}$ = 7.7 GeV. Panel (c) shows the results of the ratio (Ru/Zr) for different nuclear deformation configurations

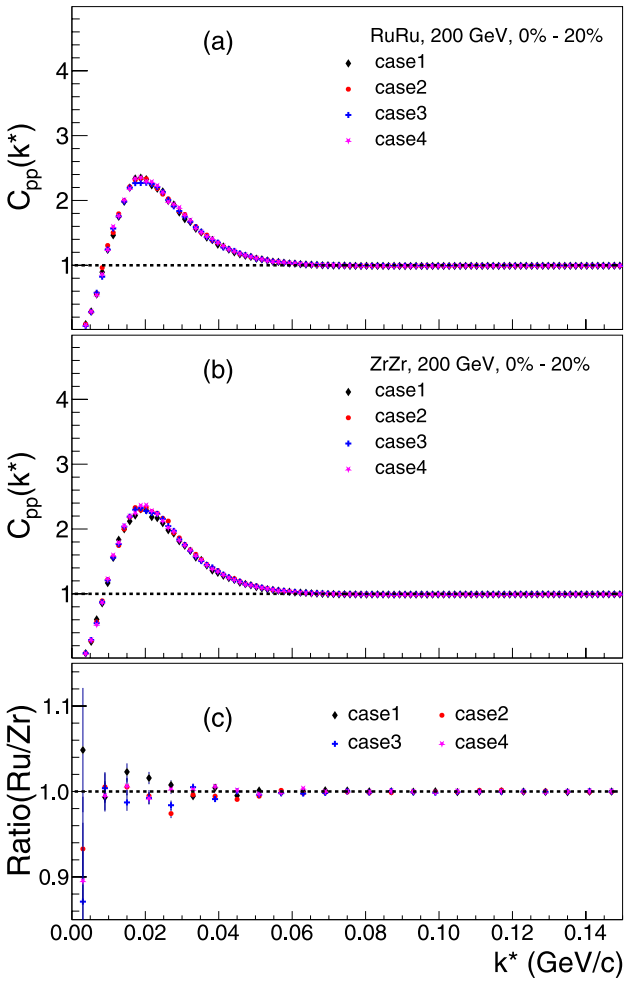

Fig. 4 Proton–proton correlation function in 0–20% central Ru + Ru (Panel a) and Zr + Zr (Panel b) collisions at $\sqrt{s_{NN}}$ = 200 GeV. Panel (c) shows the ratios (Ru/Zr) for various Woods–Saxon parameterization cases as shown in Table 1

nuclear skin and size between the isobar nuclei, also shows a maximum deviation of 2%, indicating that a thinner neutron skin induces a stronger correlation. A larger deviation from unity, reaching up to 4%, was observed in case 4, suggesting that the deformation parameter β_3 may have sizable effects on the correlation functions in peripheral collisions. By comparing the results with those of the 0–20% central collisions, a centrality dependence was revealed, with the deviation value increasing from central to peripheral collisions.

Figures 4 and 5 show the results of central and peripheral collisions at $\sqrt{s_{NN}}$ = 200 GeV for four cases of Woods–Saxon parametrization of Ru + Ru and Zr + Zr collisions. Because the source size at $\sqrt{s_{NN}}$ = 200 GeV collisions is expected to be larger than that at $\sqrt{s_{NN}}$ = 7.7 GeV collisions, the correlation functions in both central and peripheral collisions are supposed to be smaller in magnitude than those at $\sqrt{s_{NN}}$ = 7.7 GeV. In 0–20% central collisions, the ratios of the four cases are consistent with unity within statistical uncertainties at large k^* and show only tiny differences (<2%) at small k^*, indicating a negligible effect of the neutron skin and nuclear deformation on the correlation functions in central collisions at higher energies.

In peripheral collisions, the ratio (Ru/Zr) in case 1 is consistent with unity. The ratios for case 2 show deviations from unity with magnitudes similar to those at $\sqrt{s_{NN}}$ = 7.7 GeV, suggesting that the energy dependence of the ratio is relatively weak. It can be seen that the differences between the two isobaric systems caused by β_2 deformation are negligible in peripheral collisions at $\sqrt{s_{NN}}$ = 200 GeV.

We calculated the ratios of the correlation functions between different parameterization cases across the

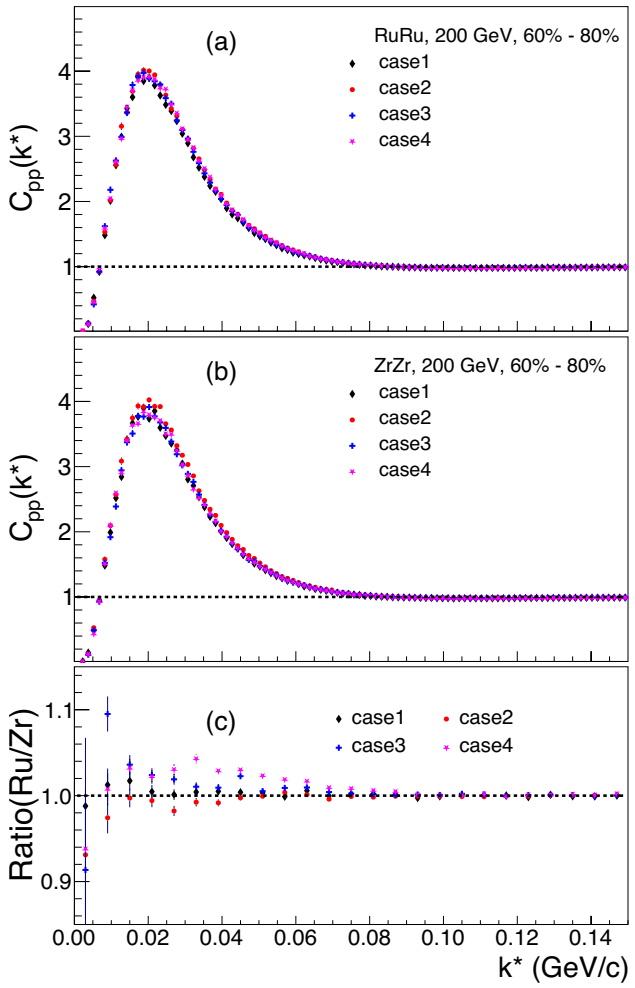

Fig. 5 Proton–proton correlation function for 60–80% central Ru + Ru (Panel a) and Zr + Zr (Panel b) collisions at $\sqrt{s_{NN}}$ = 200 GeV. The ratios (Ru/Zr) of the correlation functions between the two systems are shown in Panel (c) for different cases

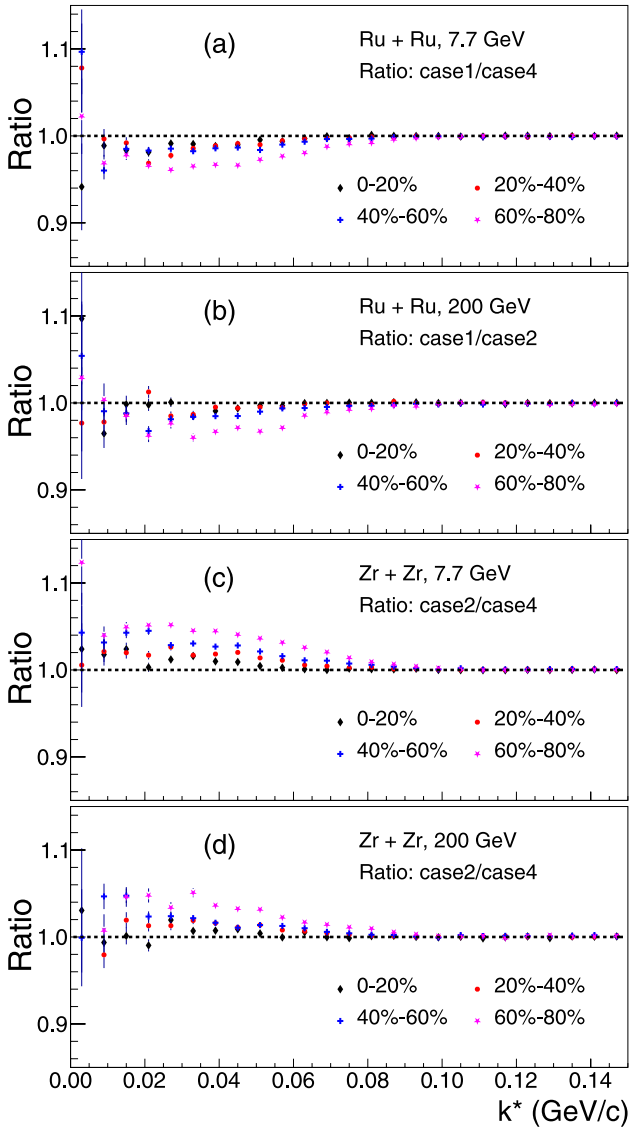

Fig. 6 Ratio of proton–proton correlation function for case 1/case 4 in Ru + Ru at $\sqrt{s_{NN}}$ = 7.7 GeV (Panel a), case 1/case 2 in Ru + Ru at $\sqrt{s_{NN}}$ = 200 GeV (Panel b), case 2/case 4 in Zr + Zr at $\sqrt{s_{NN}}$ = 7.7 GeV (Panel c) and case 2/case 4 in Zr + Zr at $\sqrt{s_{NN}}$ = 200 GeV (Panel d) in different centrality classes

centrality classes from 0–20% to 60–80%. Figure 6 shows the results for Zr + Zr and Ru + Ru collisions at $\sqrt{s_{NN}}$ of both 7.7 and 200 GeV. We find that the results show a relatively small dependence on collision energy, but exhibit significant centrality dependence. We systematically compared case 1 with case 2, case 1 with case 4, and case 2 with case 4. Through these comparisons, we quantitatively evaluated the influence of the nuclear deformation effects in the two collision systems. A maximum deviation of 4% and 5% was observed at small k^* (0.02–0.04 GeV/c) for Ru + Ru and Zr + Zr, respectively. According to the Woods–Saxon configurations in our model simulation, the deformation and neutron skin effects were found to be more pronounced in peripheral collisions, consistent with our expectations based on studies of observables such as particle yield in isobaric collision systems [64, 68].

Studies have also been performed for n-p correlation. Figures 7 and 8 show the results of central and peripheral Ru + Ru and Zr + Zr collisions at $\sqrt{s_{NN}}$ = 200 GeV. Owing to the absence of charge interactions, all the data points of the correlation function were all greater than 1. For central collisions, the correlation functions for all four cases are consistent within the statistical uncertainties, with only a tiny difference observed at small k^*. For the peripheral collisions, the differences between the n-p correlations are similar to that of p-p, indicating that the n-p pair is sensitive to the nuclear structure similar to that of the p-p pair.

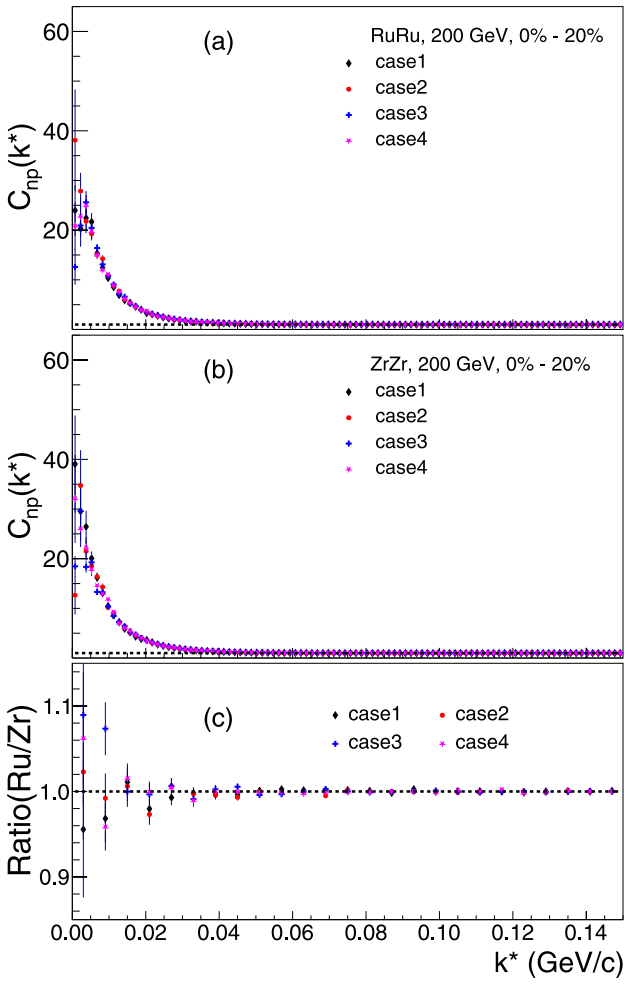

Fig. 7 Neutron–proton correlation function of 0–20% central Ru + Ru (Panel a) and Zr + Zr (Panel b) collisions at $\sqrt{s_{\mathrm{NN}}}$ = 200 GeV. The ratios (Ru/Zr) are shown in Panel (c)

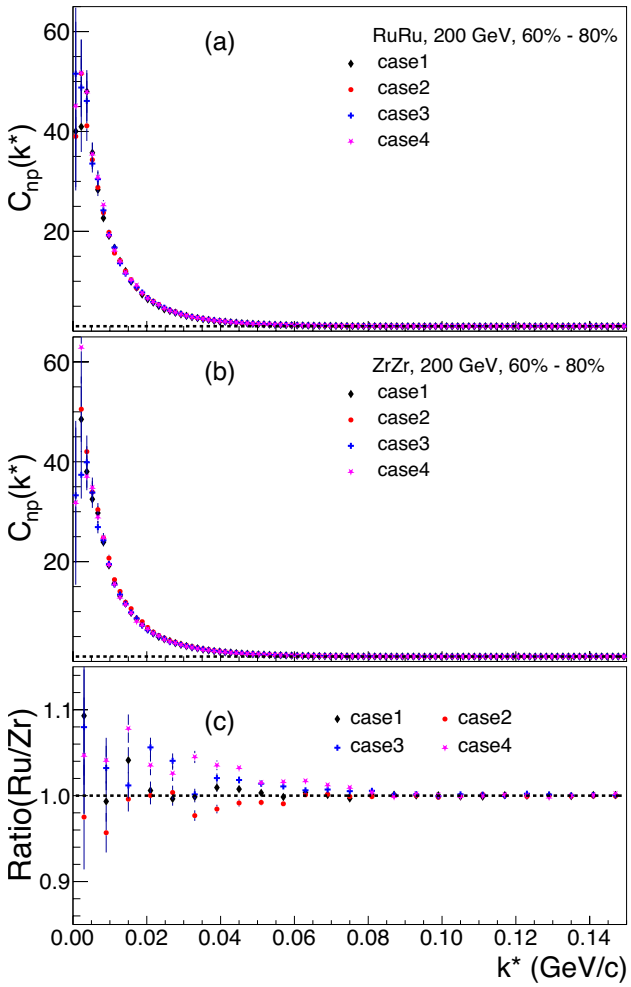

Fig. 8 Neutron–proton correlation function of 60–80% central Ru + Ru (Panel a) and Zr + Zr (Panel b) collisions at $\sqrt{s_{\mathrm{NN}}}$ = 200 GeV. The ratios (Ru/Zr) are shown in Panel (c)

The ratios of the correlation functions between the two systems (Ru/Zr) for the different cases are shown in the bottom panels of Figs. 7 and 8. It was found that the ratio results at $\sqrt{s_{\mathrm{NN}}}$ = 200 GeV were similar to the p-p correlation. No significant deviations are observed in the central collisions, indicating minimal differences between the two systems. Neither the neutron skin nor the nuclear deformation effects manifest in the correlation functions in central collisions. For peripheral collisions, similar differences to p-p correlations were observed between the four deformation cases with a maximum deviation of 4% from the unity observed, taking into consideration the statistical uncertainties. The results suggest that in n-p correlations, both the neutron skin effect and the deformation effect make non-negligible contributions. In addition, the correlation functions of both n-p and p-p show a clear centrality dependence.

4 Summary

Using the AMPT model, we investigated the nucleon momentum correlation in the relativistic collisions of Ru + Ru and Zr + Zr at $\sqrt{s_{\mathrm{NN}}}$ = 7.7 and 200 GeV. The correlation functions of p-p and n-p for different cases with various deformation parameters were calculated to quantitatively study the effects of nuclear structure and system size.

The ratios of the correlation functions between the two isobaric systems (Ru/Zr) for four different cases of Woods–Saxon parametrization were evaluated based on the simulation data with a clear centrality dependence. The ratio shows no deviation from unity in case 1 for nuclei with the same nuclear size and without deformation. We observed a deviation from unity in the ratios for cases 2–4 in both central and peripheral collisions, which could

be attributed to the deformation effect. We found that the influence of the nuclear structure becomes more significant in peripheral collisions. A maximum deviation of 5% from unity was observed between all the Woods–Saxon parameterization cases and 4% between collision systems in 60–80% peripheral collisions, incorporating nuclear size and the neutron skin effect. Meanwhile, it was found that the energy dependence of both the neutron skin effect and deformation effect in the p-p correlation is shallow. In addition, we found that in both p-p and n-p, the intensity of the correlation function in central collisions is greater than that in peripheral collisions. The results of the p-p correlation at $\sqrt{s_{\rm NN}}$ = 7.7 GeV are greater than those at 200 GeV, which reflects the fireball size produced in the corresponding collision scenarios.

Notably, our simulation study did not consider the evolution and interactions of magnetic fields related to the charge number of the colliding nuclei. Further theoretical studies incorporating magnetic field effects in nucleon momentum correlation, along with experimental measurements at RHIC energies, would enable more precise examinations of nuclear structure and size, providing stronger constraints on the nuclear structure parameters of the isobar systems [77].

Author contributions All authors contributed to the study conception and design. Material preparation, data collection and analysis were performed by Bao-Shan Xi, Jin-Hui Chen, Long Ma, Yu-Gang Ma, and Ting-Ting Wang. The first draft of the manuscript was written by Bao-Shan Xi, and all authors commented on previous versions of the manuscript. All authors read and approved the final manuscript.

Data availability The data that support the findings of this study are openly available in Science Data Bank at https://cstr.cn/31253.11.sciencedb.j00186.00746 and https://doi.org/10.57760/sciencedb.j00186.00746.

Declarations

Conflict of interest Yu-Gang Ma is the editor-in-chief for Nuclear Science and Techniques and was not involved in the editorial review or the decision to publish this article. All authors declare that there are no competing interests.

References

1. E. Shuryak, Strongly coupled quark-gluon plasma in heavy ion collisions. Rev. Mod. Phys. **89**, 035001 (2017). https://doi.org/10.1103/RevModPhys.89.035001
2. J. Adams, M. Aggarwal, Z. Ahammed et al., Experimental and theoretical challenges in the search for the quark-gluon plasma: The STAR Collaboration's critical assessment of the evidence from RHIC collisions. Nucl. Phys. A **757**, 102–183 (2005). https://doi.org/10.1016/j.nuclphysa.2005.03.085
3. K. Adcox, S.S. Adler, S. Afanasiev et al., Formation of dense partonic matter in relativistic nucleus-nucleus collisions at RHIC: experimental evaluation by the PHENIX collaboration. Nucl. Phys. A **757**, 184–283 (2005). https://doi.org/10.1016/j.nuclphysa.2005.03.086
4. A. Tumasyan, W. Adam, J.W. Andrejkovic et al., Probing charm quark dynamics via multiparticle correlations in Pb-Pb collisions at $\sqrt{s_{\rm NN}}$ =5.02 TeV. Phys. Rev. Lett. **129**, 022001 (2022). https://doi.org/10.1103/PhysRevLett.129.022001
5. Q.Y. Shou, Y.G. Ma, S. Zhang et al., Properties of QCD matter: a review of selected results from ALICE experiment. Nucl. Sci. Tech. **35**, 219 (2024). https://doi.org/10.1007/s41365-024-01583-2
6. J. Adam, D. Adamova, M.M. Aggarwal et al., Anisotropic flow of charged particles Phys in Pb-Pb collisions at $\sqrt{s_{\rm NN}}$ = 5.02 TeV. Rev. Lett. **116**, 132302 (2016). https://doi.org/10.1103/PhysRevLett.116.132302
7. C. Zhang, L. Liu, J. Chen, Probing longitudinal structures of quark gluon plasma in extreme states of nuclear matter. Sci. Sin. Phys. Mech. Astro. **55**, 1 (2025). https://doi.org/10.1360/SSPMA-2024-0571
8. M. Abdallah, B. Aboona, J. Adam et al., Search for the chiral magnetic effect with isobar collisions at $\sqrt{s_{NN}}$=200 GeV by the STAR Collaboration at the BNL Relativistic Heavy Ion Collider. Phys. Rev. C **105**, 014901 (2022). https://doi.org/10.1103/PhysRevC.105.014901
9. V. Koch, S. Schlichting, V. Skokov et al., Status of the chiral magnetic effect and collisions of isobars. Chin. Phys. C **41**, 072001 (2017). https://doi.org/10.1088/1674-1137/41/7/072001
10. W.T. Deng, X.G. Huang, G.L. Ma et al., Predictions for isobaric collisions at $\sqrt{s_{\rm NN}}$ = 200 GeV from a multiphase transport model. Phys. Rev. C **97**, 044901 (2018). https://doi.org/10.1103/PhysRevC.97.044901
11. J.H. Chen, X. Dong, X.H. He et al., Properties of the QCD matter: review of selected results from the relativistic heavy ion collider beam energy scan (RHIC BES) program. Nucl. Sci. Tech. **35**, 214 (2024). https://doi.org/10.1007/s41365-024-01591-2
12. M. Abdallah, B. Aboona, J. Adam, et al., Charge separation measurements in Au+Au collisions at $\sqrt{s_{NN}}$ = 7.7–200 gev in search of the chiral magnetic effect. arXiv:2506.00275
13. M. Abdallah, B. Aboona, J. Adam, et al., Search for the chiral magnetic effect through beam energy dependence of charge separation using event shape selection. arXiv:2506.00278
14. H.J. Xu, W. Zhao, H. Li et al., Probing nuclear structure with mean transverse momentum in relativistic isobar collisions. Phys. Rev. C **108**, L011902 (2023). https://doi.org/10.1103/PhysRevC.108.L011902
15. F. Li, Y.G. Ma, S. Zhang et al., Impact of nuclear structure on the background in the chiral magnetic effect Phys in $^{96}_{44}$Ru + $^{96}_{44}$Ru and $^{96}_{40}$Zr + $^{96}_{40}$Zr collisions at $\sqrt{s_{NN}}$ = 7.7 ~ 200 GeV from a multiphase transport model. Rev. C **106**, 014906 (2022). https://doi.org/10.1103/PhysRevC.106.014906
16. Z. Wang, J. Chen, J. Jia, et al., Multiparticle azimuthal correlations in isobaric ^{96}Ru+^{96}Ru and ^{96}Zr+^{96}Zr collisions at $\sqrt{s_{NN}}$ = 200 GeV. arXiv:2409.15040
17. J. Jia, G. Giacalone, C. Zhang, Precision tests of the nonlinear mode coupling of anisotropic flow via high-energy collisions of isobars. Chin. Phys. Lett. **40**, 042501 (2023). https://doi.org/10.1088/0256-307X/40/4/042501
18. C. Zhang, J. Jia, Evidence of quadrupole and octupole deformations in Zr96+Zr96 and Ru96+Ru96 collisions at ultrarelativistic energies. Phys. Rev. Lett. **128**, 022301 (2022). https://doi.org/10.1103/PhysRevLett.128.022301
19. B.S. Xi, X.G. Deng, S. Zhang et al., Vorticity in isobar collisions of $^{96}_{44}$ru + $^{96}_{44}$Ru and $^{96}_{40}$Zr + $^{96}_{40}$Zr at $\sqrt{s_{\rm NN}}$ = 200 GeV. Eur. Phys. J. A **59**, 33 (2023). https://doi.org/10.1140/epja/s10050-023-00932-w
20. L. Ma, Y.G. Ma, S. Zhang, Anisotropy fluctuation and correlation in central α-clustered ^{12}C +^{197} Au collisions. Phys. Rev.

C **102**, 014910 (2020). https://doi.org/10.1103/PhysRevC.102.014910
21. M.I. Abdulhamid, B.E. Aboona, J. Adam et al., Imaging shapes of atomic nuclei in high-energy nuclear collisions. Nature **635**, 67–72 (2024). https://doi.org/10.1038/s41586-024-08097-2
22. R.H. Brown, R.Q. Twiss, Correlation between photons in two coherent beams of light. Nature **177**, 27–29 (1956). https://doi.org/10.1038/177027a0
23. M. Gyulassy, S.K. Kauffmann, L.W. Wilson, Pion interferometry of nuclear collisions. 1. theory. Phys. Rev. C **20**, 2267–2292 (1979). https://doi.org/10.1103/PhysRevC.20.2267
24. D.H. Boal, C.K. Gelbke, B.K. Jennings, Intensity interferometry in subatomic physics. Rev. Mod. Phys. **62**, 553–602 (1990). https://doi.org/10.1103/RevModPhys.62.553
25. R. Lednicky, Correlation femtoscopy of multiparticle processes. Phys. Atom. Nucl. **67**, 72–82 (2004). https://doi.org/10.1134/1.1644010
26. B.S. Xi, Z.Q. Zhang, S. Zhang et al., Searching for $^{4}\overline{\mathrm{Li}}$ via the momentum-correlation function of $\bar{p}-{}^{3}\overline{\mathrm{He}}$. Phys. Rev. C **102**, 064901 (2020). https://doi.org/10.1103/PhysRevC.102.064901
27. T. Csorgo, Review of HBT or Bose-Einstein correlations in high energy heavy ion collisions. J. Phys: Conf. Ser. **50**, 259–270 (2006). https://doi.org/10.1088/1742-6596/50/1/031
28. T.T. Wang, Y.G. Ma, S. Zhang, Calculation of momentum correlation functions between π, K, and p for several heavy-ion collision systems at $\sqrt{s_{\mathrm{NN}}}$=39 GeV. Phys. Rev. C **109**, 024912 (2024). https://doi.org/10.1103/PhysRevC.109.024912
29. A.K. Pandey, Pion-kaon femtoscopy in Pb-Pb collisions Nucl at $\sqrt{s_{\mathrm{NN}}}$ = 2.76 TeV measured with ALICE. Phys. A **982**, 351–354 (2019). https://doi.org/10.1016/j.nuclphysa.2018.10.048
30. S. Acharya, D. Adamova, S.P. Adhya et al., Scattering studies with low-energy kaon-proton femtoscopy in proton-proton collisions at the LHC. Phys. Rev. Lett. **124**, 092301 (2020). https://doi.org/10.1103/PhysRevLett.124.092301
31. L. Adamczyk, J.K. Adkins, G. Agakishiev et al., Measurement of interaction between antiprotons. Nature **527**, 345–348 (2015). https://doi.org/10.1038/nature15724
32. K. Morita, T. Furumoto, A. Ohnishi, $\lambda\lambda$ interaction from relativistic heavy-ion collisions. Phys. Rev. C **91**, 024916 (2015). https://doi.org/10.1103/PhysRevC.91.024916
33. J.M. Torres-Rincon, À. Ramos, L. Tolos, Femtoscopy of d mesons and light mesons upon unitarized effective field theories. Phys. Rev. D **108**, 096008 (2023). https://doi.org/10.1103/PhysRevD.108.096008
34. K. Morita, A. Ohnishi, F. Etminan, et al., Probing multistrange dibaryons with proton-omega correlations in high-energy heavy ion collisions. Phys. Rev. C **94**, 031901 (2016). [Erratum: Phys. Rev.C 100, 069902 (2019)]. https://doi.org/10.1103/PhysRevC.94.031901
35. S. Acharya, D. Adamova, A. Adler, et al., Unveiling the strong interaction among hadrons at the LHC. Nature **588**, 232–238 (2020). [Erratum: Nature 590, E13 (2021)]. https://doi.org/10.1038/s41586-020-3001-6
36. J. Adams, M.M. Aggarwal, Z. Ahammed et al., Proton - lambda correlations in central Au+Au collisions at $\sqrt{s_{\mathrm{NN}}}$ = 200-GeV. Phys. Rev. C **74**, 064906 (2006). https://doi.org/10.1103/PhysRevC.74.064906
37. W.J. Dong, X.Z. Yu, S.Y. Ping et al., Study of baryon number transport dynamics and strangeness conservation effects using ω -hadron correlations. Nucl. Sci. Tech. **35**, 120 (2024). https://doi.org/10.1007/s41365-024-01464-8
38. L. Adamczyk, J.K. Adkins, G. Agakishiev et al., $\lambda\lambda$ correlation function in Au+Au collisions at $\sqrt{s_{NN}}$ = 200 GeV. Phys. Rev. Lett. **114**, 022301 (2015). https://doi.org/10.1103/PhysRevLett.114.022301
39. S. Acharya, D. Adamova, S.P. Adhya et al., First Observation of an Attractive Interaction between a Proton and a Cascade Baryon. Phys. Rev. Lett. **123**, 112002 (2019). https://doi.org/10.1103/PhysRevLett.123.112002
40. J. Chen, D. Keane, Y.G. Ma et al., Antinuclei in heavy-ion collisions. Phys. Rept. **760**, 1–39 (2018). https://doi.org/10.1016/j.physrep.2018.07.002
41. J. Adam, L. Adamczyk, J. Adams et al., The proton-ω correlation function in Au+Au collisions at $\sqrt{s_{NN}}$=200 GeV. Phys. Lett. B **790**, 490–497 (2019). https://doi.org/10.1016/j.physletb.2019.01.055
42. B.E. Aboona, J. Adam, L. Adamczyk et al., Light nuclei femtoscopy and baryon interactions in 3 GeV Au+Au collisions at RHIC. Phys. Lett. B **864**, 139412 (2025). https://doi.org/10.1016/j.physletb.2025.139412
43. T.T. Wang, Y.G. Ma, S. Zhang, Simulations of momentum correlation functions of light (anti)nuclei in relativistic heavy-ion collisions at $\sqrt{s_{\mathrm{NN}}}$=39 GeV. Phys. Rev. C **107**, 014911 (2023). https://doi.org/10.1103/PhysRevC.107.014911
44. S. Acharya, F.T. Acosta, D. Adamova et al., p-p, p-λ and λ-λ correlations studied via femtoscopy in pp reactions at $\sqrt{s}$ = 7 TeV. Phys. Rev. C **99**, 024001 (2019). https://doi.org/10.1103/PhysRevC.99.024001
45. M.M. Aggarwal, Z. Ahammed, A.V. Alakhverdyants et al., Pion femtoscopy in $p^{+}p$ collisions at $\sqrt{s}$ = 200 GeV. Phys. Rev. C **83**, 064905 (2011). https://doi.org/10.1103/PhysRevC.83.064905
46. S. Acharya, D. Adamova, A. Adler et al., Search for a common baryon source in high-multiplicity pp collisions at the LHC. Phys. Lett. B **811**, 135849 (2020). https://doi.org/10.1016/j.physletb.2020.135849
47. Z.W. Lin, C.M. Ko, B.A. Li et al., A Multi-phase transport model for relativistic heavy ion collisions. Phys. Rev. C **72**, 064901 (2005). https://doi.org/10.1103/PhysRevC.72.064901
48. Z.W. Lin, L. Zheng, Further developments of a multi-phase transport model for relativistic nuclear collisions. Nucl. Sci. Tech. **32**, 113 (2021). https://doi.org/10.1007/s41365-021-00944-5
49. H. Wang, J.H. Chen, Anisotropy flows in Pb–Pb collisions at LHC energies from parton scatterings with heavy quark trigger. Nucl. Sci. Tech. **33**, 15 (2022). https://doi.org/10.1007/s41365-022-00999-y
50. L. Ma, G.L. Ma, Y.G. Ma, Initial partonic eccentricity fluctuations in a multiphase transport model. Phys. Rev. C **94**, 044915 (2016). https://doi.org/10.1103/PhysRevC.94.044915
51. D. Shen, J. Chen, A. Tang et al., Impact of globally spin-aligned vector mesons on the search for the chiral magnetic effect in heavy-ion collisions. Phys. Lett. B **839**, 137777 (2023). https://doi.org/10.1016/j.physletb.2023.137777
52. D. Shen, J. Chen, Z.W. Lin, The effect of hadronic scatterings on the measurement of vector meson spin alignments in heavy-ion collisions. Chin. Phys. C **45**, 054002 (2021). https://doi.org/10.1088/1674-1137/abe763
53. L. Zhang, J. Chen, C. Zhang, Energy dependence of transverse momentum fluctuations in Au+Au collisions from a multiphase transport model. Phys. Rev. C **111**, 024911 (2025). https://doi.org/10.1103/PhysRevC.111.024911
54. C. Zhang, J. Chen, G. Giacalone et al., *Ab*-initio nucleon-nucleon correlations and their impact on high energy 16O+16O collisions. Phys. Lett. B **862**, 139322 (2025). https://doi.org/10.1016/j.physletb.2025.139322
55. X.N. Wang, M. Gyulassy, HIJING: A monte carlo model for multiple jet production in pp, pA and AA collisions. Phys. Rev. D **44**, 3501–3516 (1991). https://doi.org/10.1103/PhysRevD.44.3501
56. B. Zhang, ZPC 1.0.1: A parton cascade for ultrarelativistic heavy ion collisions. Comput. Phys. Commun. **109**, 193–206 (1998). https://doi.org/10.1016/S0010-4655(98)00010-1

57. B.A. Li, C.M. Ko, Formation of superdense hadronic matter in high-energy heavy ion collisions. Phys. Rev. C **52**, 2037–2063 (1995). https://doi.org/10.1103/PhysRevC.52.2037
58. W.T. Deng, X.G. Huang, G.L. Ma et al., Test the chiral magnetic effect with isobaric collisions. Phys. Rev. C **94**, 041901 (2016). https://doi.org/10.1103/PhysRevC.94.041901
59. G. Giacalone, J. Jia, C. Zhang, Impact of nuclear deformation on relativistic heavy-ion collisions: Assessing consistency in nuclear physics across energy scales. Phys. Rev. Lett. **127**, 242301 (2021). https://doi.org/10.1103/PhysRevLett.127.242301
60. Q.Y. Shou, Y.G. Ma, P. Sorensen et al., Parameterization of deformed nuclei for glauber modeling in relativistic heavy ion collisions. Phys. Lett. B **749**, 215–220 (2015). https://doi.org/10.1016/j.physletb.2015.07.078
61. C. Zhang, S. Bhatta, J. Jia, Ratios of collective flow observables in high-energy isobar collisions are insensitive to final-state interactions. Phys. Rev. C **106**, L031901 (2022). https://doi.org/10.1103/PhysRevC.106.L031901
62. J. Jia, C. Zhang, Scaling approach to nuclear structure in high-energy heavy-ion collisions. Phys. Rev. C **107**, L021901 (2023). https://doi.org/10.1103/PhysRevC.107.L021901
63. M. Rysavy, O. Dragoun, Tables of internal conversion coefficients for superheavy elements. Atom. Data Nucl. Data Tabl. **78**, 129–160 (2001). https://doi.org/10.1006/adnd.2001.0859
64. F. Li, S. Zhang, K.J. Sun et al., Production of light nuclei in isobaric Ru + Ru and Zr + Zr collisions at $\sqrt{s_{NN}}$=7.7-200 GeV from a multiphase transport model. Phys. Rev. C **109**, 064912 (2024). https://doi.org/10.1103/PhysRevC.109.064912
65. C. Zhang, J. Jia, J. Chen, et al., Probing the octupole deformation of ^{238}U in high-energy nuclear collisions. arXiv:2504.15245
66. H.J. Xu, X. Wang, H. Li et al., Importance of isobar density distributions on the chiral magnetic effect search. Phys. Rev. Lett. **121**, 022301 (2018). https://doi.org/10.1103/PhysRevLett.121.022301
67. H.J. Xu, H.L. Li, X.B. Wang et al., Determine the neutron skin type by relativistic isobaric collisions. Phys. Lett. B **819**, 136453 (2021). https://doi.org/10.1016/j.physletb.2021.136453
68. P. Sinha, V. Bairathi, K. Gopal et al., Effect of nuclear structure on particle production in relativistic heavy-ion collisions using a multiphase transport model. Phys. Rev. C **108**, 024911 (2023). https://doi.org/10.1103/PhysRevC.108.024911
69. R. Lednicky, V.L. Lyuboshits, Final state interaction effect on pairing correlations between particles with small relative momenta. Yad. Fiz. **35**, 1316–1330 (1981)
70. R. Lednicky, Finite-size effects on two-particle production in continuous and discrete spectrum. Phys. Part. Nucl. **40**, 307–352 (2009). https://doi.org/10.1134/S1063779609030034
71. R. Lednicky, V. Lyuboshitz, K. Mikhailov et al., Multiboson effects in multiparticle production. Phys. Rev. C **61**, 034901 (2000). https://doi.org/10.1103/PhysRevC.61.034901
72. R. Lednicky, Notes on correlation femtoscopy. Phys. Atom. Nucl. **71**, 1572–1578 (2008). https://doi.org/10.1134/S1063778808090123
73. M.A. Lisa, S. Pratt, R. Soltz et al., Femtoscopy in relativistic heavy ion collisions. Ann. Rev. Nucl. Part. Sci. **55**, 357–402 (2005). https://doi.org/10.1146/annurev.nucl.55.090704.151533
74. M.K. L. D. Landau, E. M. Lifshitz, *Nerelyativistskaya Teoriya*, 3rd Edition, (Nauka, 1974)
75. L.D. Landau, E.M. Lifshitz, *Quantum Mechanics: Non-relativistic Theory*, 3rd Edition, (Pergamon, 1977)
76. M. Abdallah, B. Aboona, J. Adam et al., Tomography of ultrarelativistic nuclei with polarized photon-gluon collisions. Sci. Adv. **9**, eabq3903 (2023). https://doi.org/10.1126/sciadv.abq3903
77. D. Shen, J. Chen, X.G. Huang et al., A review of intense electromagnetic fields. Research **8**, 0726 (2025). https://doi.org/10.34133/research.0726